Nanoscale Advances

PAPER

View Article Online
View Journal | View Issue

Cite this: *Nanoscale Adv.*, 2024, **6**, 4672

Impact of morphology and oxygen vacancy content in Ni, Fe co-doped ceria for efficient electrocatalyst based water splitting†

Abhaya Kumar Mishra,[a] Joshua Willoughby,[a] Shanna L. Estes,[b] Keliann Cleary Kohler[c] and Kyle S. Brinkman *[a]

Received 15th June 2024
Accepted 22nd July 2024

DOI: 10.1039/d4na00500g

rsc.li/nanoscale-advances

Designing a highly efficient, low-cost, sustainable electrocatalyst for the hydrogen evolution reaction (HER) and oxygen evolution reaction (OER) through water splitting is a current challenge for renewable energy technologies. This work presents a modified sol–gel route to prepare metal-ion(s) doped cerium oxide nanostructures as an efficient electrocatalyst for overall water splitting. Nickle (Ni) and iron (Fe) co-doping impacts the morphology in cerium oxide resulting in 5 nm nanoparticles with a mesoporous-like microstructure. The high level 20 mol% (1 : 1 ratio) of Ni + Fe bimetal-ion(s) doped CeO_2 shows excellent HER and OER activities compared to the monodoped Fe/Ni and pristine CeO_2. The co-doped catalysts required a low overpotential of 104 mV and 380 mV for HER and OER, respectively, in 1 M KOH, at a current density of 10 mA cm^{-2}. The Tafel slopes of 95 mV dec^{-1} and 65 mV dec^{-1} were measured for HER and OER with the same representative samples which demonstrated excellent stability even after continuous operation for 20 hours in the alkaline medium. The unique morphology, enhanced oxygen vacancy (O_v) content and the synergistic effects of dopants in CeO_2 play essential roles in enhancing the activities of Ni + Fe doped samples.

1. Introduction

Renewable energy technologies are required to address worldwide energy demands and environmental pollution issues.[1] In this regard, hydrogen fuel generated by electrochemical water-splitting is considered a promising chemical method for energy storage.[2–5] The efficiency of water electrolysis relies on the electrochemical activities of two half-reactions: the hydrogen evolution reaction (HER) at the cathode to produce hydrogen; and the oxygen evolution reaction (OER) at the anode to produce oxygen.[6–8] It is often found that HER active electrocatalysts are not suited for OER and *vice versa* due to the complexity of the reaction mechanisms.[9,10] Platinum (Pt)-based cathodes and RuO_2/IrO_2 anodes serve as current benchmarks for HER and OER activity;[11,12] however, the high cost and scarcity of these noble metal based electrodes hinder industrial applications.[13–16] Additionally, during water splitting, catalysts can undergo dissolution and redeposition, leading to electrode cross-contamination, which requires increased energy input to maintain desired reaction rates, significantly raising operational expenses.[17] Therefore, cost-effective, efficient, noble-metal-free electrocatalysts for both the HER and OER is a priority need for renewable energy technology.

In this context, cerium oxide (CeO_2, ceria), a rare earth metal oxide, is an ideal model system to explore the impact of dopants on oxygen vacancy (O_v) content and microstructure. Moreover, the ratio of Ce^{4+}/Ce^{3+} in CeO_2 controls the ionic/electronic conductivity, and O_v creation.[18–21] Increased co-doping of CeO_2 nanostructures may introduce a significant number of defects, leading to surface alteration, substantial changes in the local coordination of atoms, and a modified electronic environment, all of which may contribute to regulate work function for optimizing catalyst performance.[22,23] It was reported that various bimetal cation(s), such as (Co + Cu), (Cu + Fe), (Cu + Mn), (Cu + Ni), *etc.*, as co-dopants in the CeO_2 nanostructure enhance electrochemical, catalytic, and photocatalytic activity.[24–28] Therefore, strategically selecting a combination of metal ions for co-doping into the lattice of CeO_2 nanostructures could enhance water-splitting activities.

Traditionally, 3d transition metal cation(s) are employed as co-dopants in HER and OER electrocatalysts because of their suitable ionic size and redox activity.[29–31] Among the various 3d transition metal ions, Ni and Fe are the primary choices as dopants to enhance the electrochemical water splitting activities.[32–34] For example, Hai *et al.* found that Ni, Fe co-doped

[a]*Department of Materials Science and Engineering, Clemson University, Clemson, SC 29634, USA. E-mail: ksbrink@clemson.edu*

[b]*Department of Environmental Engineering and Earth Sciences, Clemson University, Anderson, SC 29625, USA. E-mail: sestes@clemson.edu*

[c]*Advanced Materials Research Laboratory (AMRL), Clemson University, Anderson, SC 29625, USA. E-mail: kelliak@clemson.edu*

† Electronic supplementary information (ESI) available. See DOI: https://doi.org/10.1039/d4na00500g

$W_{18}O_{49}$ grown on nickel foam boosted water splitting activities.[35] At present, no reports are available on Ni and Fe as co-dopants in nanostructured CeO_2 for bifunctional HER and OER activities. A number of synthesis methods are available for fabrication of Ni, Fe co-doped CeO_2, including hydrothermal, coprecipitation, sol–gel, and flame-made.[36–39] Among the above methods, sol–gel synthesis has attracted the most attention because it yields homogenous distribution of dopants. Dopant contents in ceria ranging from 5–30 at% have been achieved using sol–gel synthesis, with maximum O_v achieved for CeO_2 doped with 10 at% of Fe.[40–42]

The present study aims to evaluate the impact of up to 20 mol% Ni, Fe and Ni + Fe co-doping on the electrochemical activity of CeO_2 for water splitting. A modified sol–gel method was employed to synthesize pristine, (10 + 10) mol% Ni + Fe, as well as 20 mol% of Ni and Fe metal cation(s) doped CeO_2 nanostructure. The novelty of the present work lies in preparing the catalysts without the involvement of a surfactant to control the size and acid/base to adjust the pH. The synthesis method is highly flexible and associated with a single step to introduce a high amount 20 mol% of co-doped cation(s) into the host matrix in the aqueous medium. The absence of impurity phases and uniform distribution of dopant(s) are discussed based on XRD and TEM-HRTEM results. Further, Raman spectroscopy was utilized to quantify the enhanced concentration of O_v in doped catalysts. Finally, the as-synthesised catalysts for HER and OER were evaluated by linear sweep voltammetry (LSV), cyclic voltammetry (CV), potentiostatic impedance (EIS), and chronoamperometry (*i*–*t*). The HER and OER activity of as-synthesized materials were compared from the overpotential required to achieved current density 10 mA cm^{-2}, which is equivalent to 10% solar-to-fuel conversion efficiency.[43] The present work controlled the size of co-doped CeO_2 into 5 nm nanoparticles with a mesoporous microstructure that exhibits higher HER and OER activities as compared to mono-doped (Ni/Fe) and pristine CeO_2.

2. Experimental section

2.1. Chemicals

Cerium nitrate hexahydrate $Ce(NO_3)_2 \cdot 6H_2O$, nickel(III) acetate hydrate, iron(III) nitrate nonahydrate, ethylene diamine (ED), ethylenediaminetetraacetic acid (EDTA), all from Thermo Scientific; *N*-methyl-2-pyrrolidone (NMP) from TCI, and nickel foam from MSE Supplies were analytical grade and used without modification.

2.1.1. Synthesis of pristine CeO_2. A simple modified sol–gel route was employed to synthesize pristine CeO_2 nanostructures.[44] The water-assisted sol–gel method involved a combination of organic molecules [ethylenediamine tetraacetic acid (EDTA) and ethylenediamine (ED)], and metal precursor salt in the molar ratio of 1 : 3 : 1, respectively. The soluble EDTA-ED combination undergoes condensation reactions to form polymeric gel during heating. The EDTA-ED combination and the condensation process entrap dopants and host metal cations in the organic framework *via* coordinate bonding. Consequently, the metal cation(s) distribute uniformly, facilitating their incorporation into the doped host lattice during subsequent annealing steps. In brief, 0.292 g of EDTA (1 mmol) was mixed with 25 mL of water in a 200 mL beaker. To the EDTA-water mixture, 200 μL (3 mmol) ED was added with continuous stirring at 300 rpm to obtain a clear solution. Then, the required amount of cerium precursor salt (1 mmol) dissolved in 25 mL of water was added to the EDTA-ED solution drop by drop. The above sol solution was kept at 70 °C to form a polymeric-like gel. The above gel was heated at 200 °C for 2 h to form a voluminous carbonaceous material, which was finally calcined at 450 °C for 5 h to obtain the desired CeO_2 nanostructure.

2.1.2. Doping of mono- (Ni, Fe) and bi (Ni + Fe)-cation(s) into CeO_2. The mono-Ni, Fe, and bi-cation(s) (Ni + Fe) doped CeO_2 nanostructures were prepared using a similar sol–gel method with marginal modification. Based on earlier literature, 20 mol% of Ni + Fe co-doping into CeO_2 was chosen to benefit from the combination effect of dopant, more oxygen vacancy, surface alternation while maintaining the material's structural integrity. To achieve the high level of dopant(s) (20 mol%), the stoichiometric amounts of precursor salts (8 : 2 (Ce : Fe/Ni) and 8 : 1 : 1 (Ce : Ni : Fe)) were dissolved in 25 mL water to give 1 mmol of total cations, *i.e.*, dopant(s) (Ni, Fe)/(Ni + Fe) + host (Ce).

2.2.1. Materials characterization. The as-synthesized materials were analysed in detail to study the structural, morphological, and electrochemical activities. The Rigaku Smart Lab X-ray diffractometer was used to obtain the powder X-ray diffraction patterns that used monochromatic Cu Kα (1.5406 Å), 40 kV, radiation, and the data were collected in a 2θ angular range of 10–80. Raman spectra for each dried and ground ceria powder were collected at room temperature using a Renishaw inVia Qontor Raman microscope with a circularly polarized excitation line of 532 nm. The microstructure of pristine and Ni + Fe co-doped CeO_2 catalyst were analysed with transmission electron microscope (TEM) (Hitachi H9500) operating at 300 kV. The HAADF-STEM elemental mapping of Ni + Fe co-doped samples was carried out with (Hitachi SU9000), 30 kV. The surface elemental composition and chemical states of the representative sample were examined using X-ray photoelectron spectroscopy (XPS) with a PHI Versaprobe III, equipped with monochromatic Al Kα X-ray radiation source ($h\nu = 1486.6$ eV), powered at 25 W and 15 kV. Survey scans used a step size of 0.8 eV, dwell time of 50 ms, and pass energy of 224 eV. High resolution scans were an average of three sweeps, each collected with a step size of 0.125 eV, dwell time of 100 ms, and pass energy of 140 eV.

2.2.2. Electrochemical study. All the electrochemical tests were evaluated using Gamry instruments reference 620 in 1 M aqueous KOH electrolyte. The catalysts modified nickel foam, Pt wires, and saturated calomel electrode (SCE) were used as working, counter, and reference electrodes, respectively, in a conventional three-electrode system. Prior to drop casting, the nickel foam was cleaned in a 3 M HCl to remove the possible oxide, hydroxide impurities on its surface. The electrocatalyst ink was prepared by taking 10 mg of the active catalyst and 1 mg of PVDF as binder in 1 mL of NMP solvent. After the sonication

treatment of 1 h, 200 μL of the homogeneous the ink was drop cast on to into the washed nickel foam, and dried at 80 °C for 4 h to evaporated the solvent. The HER, OER performance were determined from the LSV data collected in the cathodic and anodic regime. The LSV data were converted into the reversible hydrogen electrode (RHE) scale using the eqn (i)

$$E_{RHE} = E^{0}_{SCE} + E_{SCE} + 0.0594\ pH \quad (i)$$

Here E_{RHE} is the potential in RHE scale, $E^{0}_{SCE} = 0.241$ V is the standard potential of SCE, and E_{SCE} is the working potential *versus* (*vs.*) SCE.[45] The OER overpotential (η_X) required to achieve the current density X (numerical value) mA cm^{-2} was calculated from the equation $\eta_X = E$ (*versus* RHE) − 1.23 V. Similarly, EIS spectra were recorded to know the charge transfer phenomenon at the electrode–electrolyte interface by applying DC voltage −0.2 and 1.56 V *vs.* RHE in the in the frequency range 100 kHz to 0.1 Hz with ac perturbation of 0.01 V. All of the characteristic LSVs data were corrected with 100% of *iR* compensation by using the EIS data. The *iR* compensations for HER and OER are stated as[46]

$$E_{corrcted} = E_{exp} - E_{iR} = E_{RHE} - (I_{mea} \times R_s)$$

Here $E_{corrcted}$ represent *iR* corrected potential, E_{exp} indicates experimentally measured potential, I_{mea} and R_s are the measured current and the contact resistance between electrode and solution.

3. Results and discussion

3.1. Structural properties

The crystal structures and different phases of as-synthesized materials were evaluated from the recorded PXRD patterns. Fig. 1a shows the XRD data of 20% of Ni, Fe mono-doped, equimolar Ni + Fe co-doped, and pristine CeO_2 powder samples. The diffraction peaks of the undoped samples are well-matched to the cubic fluorite structure of CeO_2, indicating that as-synthesized catalysts have no impurities within the detection limits. The observed individual peak positions were indexed according to the reference pattern JCPDS card no. 01-080-6915. No additional peaks were noticed from the doped metal-ion(s) precursor. However, a shift and broadening in the peaks were found by introducing dopants, as evidenced by the magnified (111) and (200) peak positions shown in Fig. 1b. As seen, the increase in full-width at half maximum (FWHM) with the addition of Ni/Fe and Ni + Fe heteroatom (s) may be due to uniform doping, resulting in a reduction in the coherence of crystalline regions which is also reflected in high-resolution TEM images (Fig. 3f). It is expected that metal cation(s) Ni^{2+} (0.69 A)[47] and Fe^{3+} (0.79 A)[48] introduction into the CeO_2 to replace higher oxidation state Ce^{4+} would results in an significant change in the two theta value resulting from lattice contraction/extension.[49] However, insignificant change in the lattice parameter were observed owing to change in the ratio of Ce^{3+} to Ce^{4+} along with creation of O_v. Table 1 highlights the physicochemical properties of the catalysts.

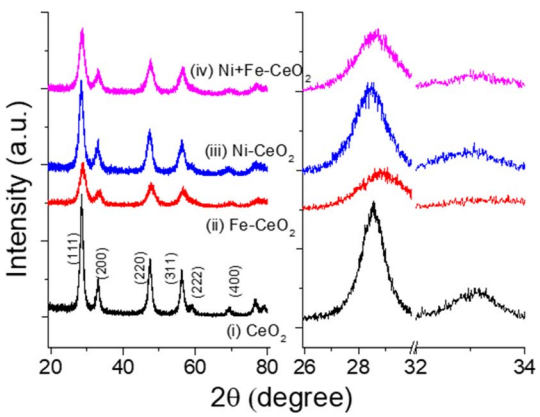

Fig. 1 Powder X-ray patterns of (a) undoped, Ni, Fe doped, and (Ni + Fe) co-doped CeO_2 catalyst. (b) Enlarged view of (111) and (200) facets of the corresponding diffraction patterns.

3.2 Raman analysis

Raman spectroscopy analysis of the catalysts was carried out to understand the effect of doping into the CeO_2 lattice framework. Fig. 2a displays the Raman spectra of undoped, mono, and co-doped CeO_2 samples. The Raman spectra of pure CeO_2 samples show a band at 462 cm^{-1} corresponding to a triply degenerate symmetrical stretching band (F_{2g}) of CeO_2 fluorite structure.[50] A significant shift towards higher wavenumber along with broadening was noticed for F_{2g} bands for the other samples, indicating the doping of metal ion(s) into the CeO_2 lattice unit, in agreement with the observed XRD results (Fig. 1b).[51,52] Changes in the intensity and frequency of F_{2g} bands evidence the interaction between dopant(s) and host CeO_2. In addition, a small defect induced band (D) at 602 cm^{-1} was observed, which is due to Raman selection rules associated with defects of CeO_2, particularly oxygen vacancies.[49,53] In the CeO_2 structure, Ce ions exist in either 3+ or 4+ oxidation states therefore the introduction of aliovalent ion(s), such as Ni^{2+} and Fe^{3+}, leads to symmetry breaking. As a result, to maintain the charge neutrality in the ionic crystal, a larger size of Ce^{3+} and an oxygen vacancy are formed.[54] The ratio of D and F_{2g} band intensities (I_D and I_{F2g} respectively) were utilized to estimate the oxygen vacancy concentration. The values of $I_d/I_{F_{2g}}$ of the as-synthesized catalysts follow the trends Ni + Fe-CeO_2 > Ni-CeO_2 > Fe-CeO_2 > CeO_2. It is seen that the Ni + Fe co-dopant generates more oxygen vacancies than Ni and Fe mono-doped CeO_2 at the same 20 mol% doping level. The optimal Fe content (10 mol%) in Ni + Fe doped CeO_2 may exhibits charge compensation mechanism, which involve extrinsic and intrinsic point defects.[55] Kroger–Vink notation is adopted to describe the process shown below:[56]

$$Fe_2O_3 + CeO_2 \rightarrow 2Fe'_{Ce} + V^{\cdot\cdot}_{O} + O^{\times}_{O} \quad (ii)$$

$$O^{\times}_{O} + 2Ce^{\times}_{Ce} \rightarrow 2Ce'_{Ce} + 1/2O_2 + V^{\cdot\cdot}_{O} \quad (iii)$$

Here, (ii) and (iii) represents extrinsic and intrinsic oxygen vacancies formation reactions respectively. In the above

Table 1 Physicochemical properties of the catalysts

Catalysts	Unit cell side length (A)	CeO_2 crystallite size[a] (nm)	CeO_2 particle size[b] (nm)
CeO_2	5.419	7.97	10
Ni-CeO_2	5.418	5.70	—
Fe-CeO_2	5.409	4.16	—
Ni + Fe-CeO_2	5.408	4.79	5

[a] XRD results at plane (111) 28.5 (2 theta). [b] TEM analysis.

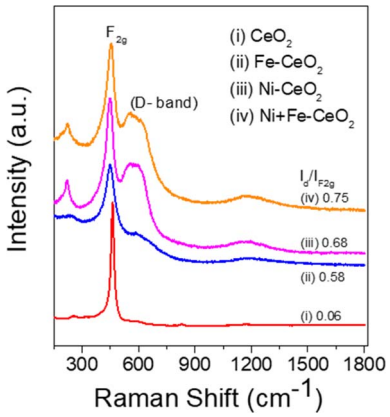

Fig. 2 Raman spectra of as-synthesized materials.

equation $Ce_{Ce}^{\times}$, and $Ce_{Ce}^{'}$ are the Ce^{4+}, and Ce^{3+} on cerium lattice sites of CeO_2, $O_O^{\times}$ is the O^{2-} ion on oxygen lattice sites, and $V_O^{\cdot\cdot}$ represents the formation of oxygen vacancy in CeO_2 release two free electron. However, higher levels of Fe dopants in excess of 10 mol% may result in an interstitial compensation mechanism.[57,58]

$$2Fe_2O_3 + CeO_2 \rightarrow 3Fe_{Ce}^{'} + Fe_i^{\cdots} + 6O_O^{\times} \quad \text{(iv)}$$

In this scenario, three Fe^{3+} ions substitute four Ce^{4+} with charge neutrality accomplished by Fe^{3+} in the interstitial sites of the fluorite cubic sites of CeO_2.[59] Overall, this resulted in a decreased O_v content with higher doping of Fe^{3+} in doped CeO_2 nanocrystals.[60–63] For example, Bao *et al.* reported that doping at 10% Fe resulted in elevated O_v vacancy content which become almost zero at higher doping levels near 50 at% Fe.[64]

3.3. Microstructure

The microstructural features of the representative pristine CeO_2 and Ni + Fe-CeO_2 co-doped materials were evaluated by bright field TEM and HR-TEM images. Fig. 3(a and b) represents the TEM images of the pristine CeO_2. As seen, pure CeO_2 (Fig. 3a) exhibits a nanosheet-like morphology. Moreover, the magnified TEM images (Fig. 3b) confirmed that uniform nanoparticles with an average size of 10 nm were integrated to form the above-mentioned architecture. The high-resolution TEM images were collected from the region highlighted as green circles in the corresponding magnified TEM (Fig. 3c). The interplanar distance (d) value of 0.30 nm confirmed that the (111) facet of the CeO_2 nanosheet is highly exposed, which is also seen as a highly intense peak in XRD patterns. It is seen in Fig. 3d that Ni + Fe-CeO_2 exhibits mesopores like features. The average particle size of Ni + Fe doped samples were found to of 4–5 nm (Fig. 3e), which is half of the pristine CeO_2. This observation indicates that the doping-induced change in the morphology of the pristine CeO_2 nanosheet. Kumar *et al.* also reported the synthesis of similar mesoporous cerium oxide (CeO_2) nanostructures by macroalgae polymer mediated approach.[65] The short-range lattice arrangement evident from the HRTEM images shown in the Fig. 3f. In the HRTEM images coherence of crystalline regions are marked by dotted circles. The selected area electron diffraction (SAED) pattern shown as inset in Fig. 3f also support the single-phase nature of the Ni + Fe co-doped CeO_2 mesoporous structure. This suggests the presence of Ni^{2+}, and Fe^{3+} cation(s) as co-dopants has an impact on in the coherence of crystalline regions of doped CeO_2 nanocrystals. The dramatic decreasing in the particle sizes offer more available sites for electrode/electrolyte interactions leading to higher electrochemical activities.

The elemental mapping from high-angle annular dark-field scanning TEM (HAADF-STEM) of Ni + Fe-CeO_2 samples is shown in Fig. 4. The analysis clearly indicates uniform distribution of Ni, Fe, Ce and O in mesoporous CeO_2. Therefore, the Ni + Fe-CeO_2 co-doped catalyst with 20 mol% at 1 : 1 ratio of dopant(s) may affiliate with multiple bonding environments such as Ce–Fe–O, Ce–Ni–O, and Ce–Fe–Ni–O. These changes in the local atomic arrangement results in favourable sites for the multistep electrochemical water splitting reaction.

3.4. X-ray photoelectron spectroscopy

XPS analysis was carried out to investigate the surface composition and chemical states of the CeO_2 nanosheet. The survey spectrum from XPS shown in Fig. S1† confirmed the presence of Ce, O, and carbon C. The region XPS spectra for Ce 3d, O 1s, are shown in Fig. 5a–c. The deconvoluted Ce 3d spectra in Fig. 5a shows multiplet peaks arising from the spin orbit coupling of Ce $3d_{5/2}$ and Ce $3d_{3/2}$ core level, respectively.[66] The peaks in the high binding energy (BE) range 880–900 eV are ascribed to Ce $3d_{5/2}$ and the peak located in the range 900–920 correspond to Ce $3d_{3/2}$.[67] The prominent photoelectron features at BE of 882.5, 888.9, and 898.1 eV signifies $3d_{5/2}$ for Ce^{4+}, while that at 901.1, 907.6, and 916.7 eV correspond to $3d_{3/2}$ level of Ce^{4+}.[68] Similarly, the doublets at BE 880.9 and 885.2 eV is assigned to the Ce^{3+} $3d_{5/2}$ level, while the peaks at 899.4 and 903.6 eV are correspond

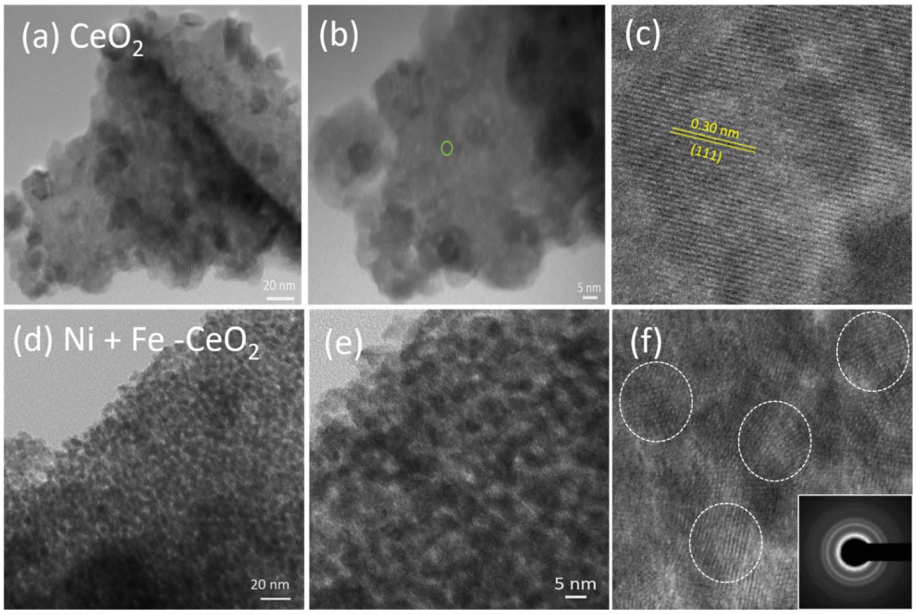

Fig. 3 TEM and HRTEM images of (a–c) pristine CeO_2, (d–f) 20 mol% Ni + Fe at 1 : 1 ratio doped CeO_2.

to Ce^{3+} $3d_{3/2}$.[69] This indicated the presence of Ce^{3+}, and Ce^{4+}, oxidation sate in CeO_2. The corresponding O 1s spectra is displayed in Fig. 5b. The feature of O 1s showing peaks different binding energy due to different electronic environment. Experiments on doped and co-doped samples showed minimal impact on the shape or intensity of the XPS signal of the Ce 3d bands.[40] The Ni 2p and Fe 3p region XPS spectra of Fe and Ni dopant in the Ni + Fe co-doped CeO_2 sample are shown in Fig. S2.† The fitting peak of Ni 2p at 855.1 eV and 856.2 eV (Fig. S2a†) are attributed to +2 and +3 state of Ni. Strong satellite peak of Ni at 861.2 eV was also observed.[70] The peaks at 55.4 eV and 56.7 eV (Fig. S2b†) in Fe 3p correspond to +3 and valence +4 oxidation states.[71] The XPS analysis confirmed the presence of high valence Fe^{4+} and Ni^{3+} ions in co-doped samples crucial for achieving superior electrocatalytic water splitting activity.

3.5 Electrochemical activities

The impact of 20 mol% Ni/Fe and (Ni + Fe) at 1 : 1 dopant-(s) in CeO_2 on the electrochemical activity were examined by a range of tests including LSV, *i–t*, CV, and EIS. All the tests were carried out in a three-electrode configuration under identical test conditions with 1 M KOH aqueous solution as the electrolyte. It is noted that the LSVs data were recorded at a slow sweep rate of 1 mV s^{-1} to minimize the capacitive current.[72] Fig. 6a displays the HER-LSV curves of all doped and pristine CeO_2 along with bare nickel foam for comparison.

As seen from Fig. 6a, the bare nickel foam exhibits a high overpotential of (270 mV *vs.* RHE) to achieve (10 mA cm^{-2}) current density, indicating the minor contribution for HER activities. The sharp distinctions of LSV curves with higher cathodic current densities for Ni, Fe, and Ni + Fe dopant(s) in CeO_2 nanocrystal suggest the importance of employing

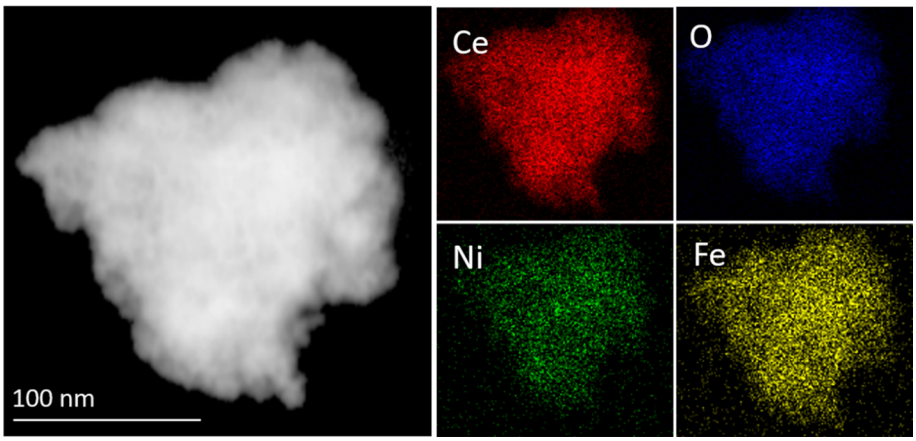

Fig. 4 HAADF-STEM image, and elemental mapping showing Ce, O, Ni, and Fe in CeO_2 mesoporous.

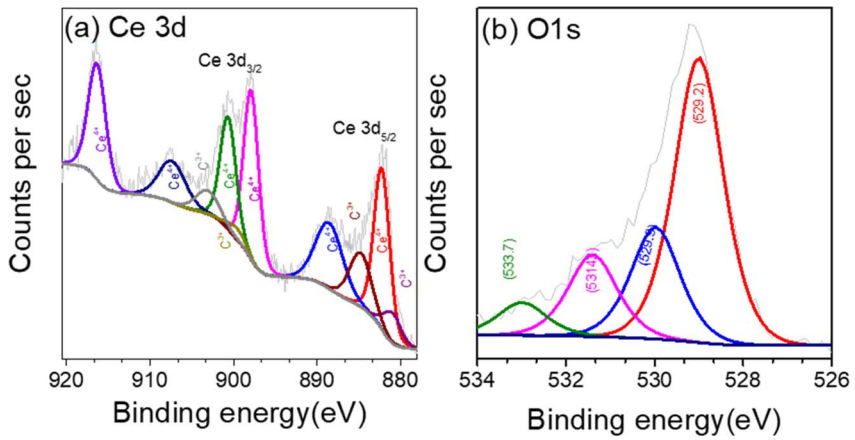

Fig. 5 (a) Region XPS spectra of CeO_2 nanoparticles (a) Ce 3d (b) O 1s.

a catalyst on the bare nickel foam. CeO_2, Ni, Fe, Ni + Fe doped(s) exhibited overpotentials of 198 mV, 123 mV, 157 mV, and 104 mV respectively at the 10 mA cm^{-2} current density associated with optimized solar to fuel conversion efficiency. The lower overpotential and higher current density of Ni + Fe doped CeO_2 catalyst compared to the other prepared electrodes as well as literature (Table 2) suggest superior HER activity. The excellent HER activities of the Ni + Fe CeO_2 electrode are ascribed to the unique mesoporous morphology that creates more active sites and greater O_v point defect concentration.

The HER kinetics and the reaction mechanism observed at the electrode surface were measured by the Tafel slope.[82] Fig. 6b exhibits the Tafel plots, and the Tafel slope of the samples are obtained from the linear fit of potential *versus* log $|i|$. The co-doped CeO_2 electrocatalyst exhibits considerably smallest Tafel value (93 mV dec^{-1}), whereas the pristine CeO_2 show higher Tafel value (150 mV dec^{-1}) among all synthesized materials. The Tafel slope value of the Ni/Fe doped electrodes were found to 120/132 mV dec^{-1}. A smaller Tafel slope reflects a kinetically favoured electrode reaction and higher HER activities. The HER histograms of Tafel slope and overpotential η_{10} (Fig. S3a†) for all electrodes suggest that it follows the Volmer–Heyrovsky mechanism in the alkaline medium as following steps.[83]

$$\text{Volmer steps: } H_2O + e^- \rightarrow OH^- + H_{ads}$$

$$\text{Heyrovsky step: } H_2O + e^- + H_{ads} \rightarrow OH^- + H_2$$

The Volmer step in an alkaline medium involves water reduction to adsorbed H (H_{ads}) on active catalyst sites, while the Heyrovsky step corresponds to the desorption of H_{ads} to generate a hydrogen molecule. In the Volmer–Heyrovsky mechanism, the Tafel slope value of 118 mV dec^{-1} suggests the Volmer step is the rate-determined step (RDS), while 40 mV dec^{-1} represents the Heyrovsky step as RDS.[84] The observed HER Tafel slope value 93 mV dec^{-1} of Ni + Fe co-doped CeO_2 mesoporous catalyst suggests that it follows the Volmer–Heyrovsky mechanism, with the Volmer step being the RDS.

The long-term stability test of the electrodes is an important parameter for industrial application. The stability tests of Ni + Fe-CeO_2 (best HER performance electrocatalyst) was evaluated by conducting chronoamperometry test (Fig. 6c) at the overpotential of 104 mV *vs.* RHE, and 180 mV *vs.* RHE, respectively for 20 h. It is to be observed that an insubstantial change in current density 2.27%, and 2.38% at 104 mV, and 180 mV, were found even after 20 h of prolonged continuous operation.

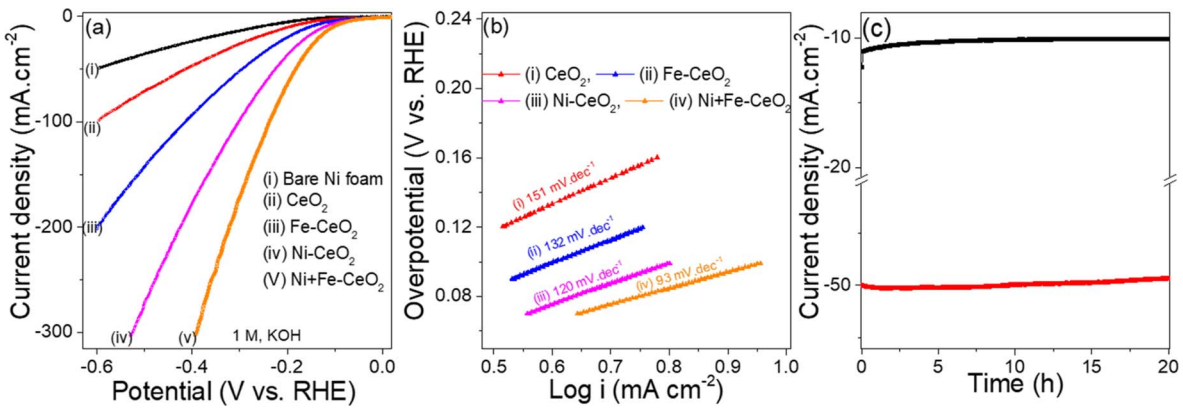

Fig. 6 (a) HER LSV curves (b) Tafel slope for HER, (c) HER *i*–*t* tests.

Table 2 Comparison of HER and OER electrochemical parameters in CeO_2 based electrocatalysts

	HER		OER		
Active materials	Overpotential (mV)	Tafel slope (mV dec^{-1})	Overpotential (mV)	Tafel slope (mV dec^{-1})	Ref.
$CeO_2/Ce(OH)_2$	317	140	410	66	73
CeO_2-$NiSe_2$	130	115	—	—	74
$gC_3N_4/CeO_2/Fe_3O_4$	310	102	400	74	75
Gd-CeO_2	99	183	369	211	76
Cu supported Ni-P/CeO_2	118	122	—	—	77
20% GDP-PBC	—	—	420	79	78
CeO_2/Ni/NC	320	150	390	123	79
Mo_2C/CeO_2/NC	220	123			80
CeO_2/Co@NCH	520	145	479	149	81
20% Ni + Fe-CeO_2	**104**	**93**	**380**	**65**	**This work**

The improvement of HER in co-doped CeO_2 nanostructure can be attributed to (i) The unique mesopores formed with 20 mol% of Ni + Fe at 1 : 1 dopant(s) (Fig. 2c and d) results in an increased number of active sites for electrode/electrolyte interaction (ii) surface alteration, changes in the local coordination of atoms along with the formation of O_v enhances the adsorption and desorption of the intermediates during the electrolysis and (iii) Ni, Fe bimetal cation(s) with different oxidation states and atomic size impact the local conductivity and charge density, resulting in faster charge transfer.[85]

Similarly, the OER activities of as-synthesized electrodes were measured in the same three electrode configuration under 1 M KOH electrolyte solution. The LSV plots representing OER are collected at a scan rate of 1 mV s^{-1} and display in the Fig. 7a. The overpotential required to achieve a current density of 10 mA cm^{-2} follows the sequence of Ni + Fe co-doped (380 mV) < Fe-CeO_2 (420 mV) < Ni-CeO_2 (450 mV) < CeO_2 (470 mV), respectively. Among the examined electrodes, the Ni + Fe-CeO_2 sample shows notably low overpotential 380 mV at a current density of 10 mA cm^{-2}, and the result is comparable to overpotentials required for other CeO_2 based electrocatalysts such as Ru/CeO_2 (420 mV),[86] CeO_2/Co@N-doped carbon (474 mV),[87] and CeO_2/CuO (410 mV).[88] The Ni + Fe co-dopant in other catalysts systems has demonstrated an increase in the OER activity. For examples, Tuo *et al.* found from DFT modelling efforts that Ni + Fe co-doped $CoSe_2$ shows a higher OER rate than Fe, Ni mono-doped catalyst.[89] Recently Paladugu *et al.* demonstrated that 50% rare earth cation substitution for Ce in CeO_2 created oxygen vacancies in the host lattices resulting in a decrease in the adsorption energy of the OH intermediate in OER.[90] Yu *et al.* reported that CeO_{2-x}-FeNi catalysts showed a higher OER performance than CeO_{2-x}-Ni and CeO_2-FeNi due to formation higher valence Ni cations in the Ni, Fe doped system.[91] Tafel plots for all samples were collected to quantify the reaction kinetics as shown in the Fig. 7b. The Tafel slope found for Ni + Fe-CeO_2 was 65 mV dec^{-1} which is lower than those Fe-CeO_2 (85 mV dec^{-1}), Ni-CeO_2 (98 mV dec^{-1}), and pristine CeO_2 (168 mV dec^{-1}), respectively. The histograms of Tafel slope and overpotential η_{10} (Fig. S3b†) show lower overpotential (η_{10}) and faster kinetics for 20 mol% Ni + Fe co-doped mesoporous CeO_2, indicating superior OER performance. The OER activities were also comparable to other doped CeO_2 based system listed in the Table 2. The Fig. 7c show the *i*–*t* results of Ni + Fe doped samples performed at 1.6 V and 1.7 V, respectively. After 20 h chronoamperometry measurement, a small change in current density was observed for both applied constant potential

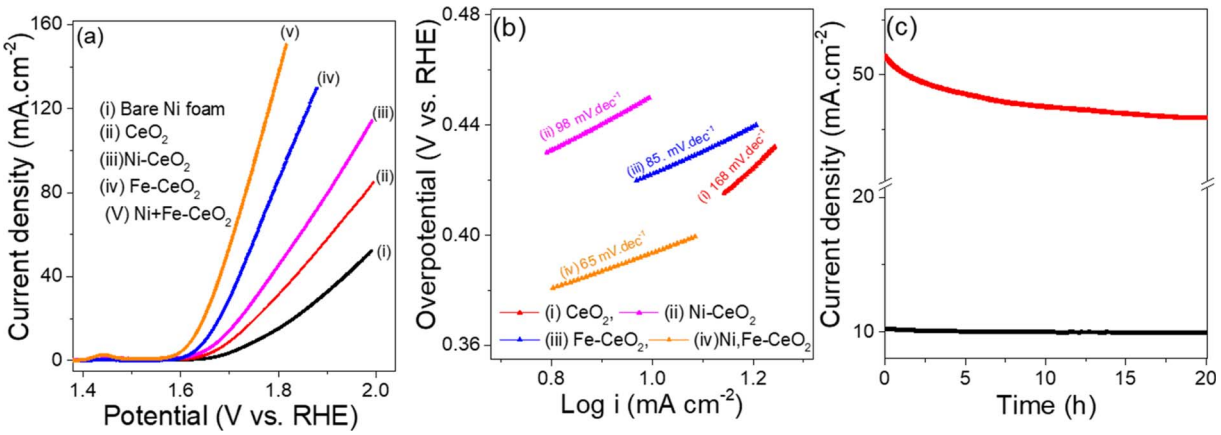

Fig. 7 (a) OER LSV curves (b) Tafel slope for OER, (c) OER *i*–*t* tests.

indicating excellent stability for this composition. Furthermore, the microstructure of the Ni + Fe co-doped CeO_2 sample was investigated by TEM after the *i–t* tests carried out under HER and OER conditions for 20 hours at 10 mA cm^{-2} and 50 mA cm^{-2}, respectively. The mesoporous like structure of Ni + Fe codoped CeO_2 samples (Fig. S4†) was found to be remain similar to the original material (Fig. 3d) suggesting high stability of the electrode catalyst.

To understand the higher HER and OER activities of Ni + Fe doped CeO_2 mesopores electrode, the electrochemically active surface area (EASA) depicting active sites for all catalysts was measured. The EASA was estimated by the formula (v)[92]

$$\text{EASA} = C_{dl}/C_s; \quad \text{(v)}$$

C_s is the specific electrochemical double-layer capacitance of an atomically smooth planer surface. The value of C_s varies between 0.020 and 0.060 mF cm^{-2} in an alkaline medium, and here is taken as 0.04 mF cm^{-2}.[43] C_{dl}, is the electrochemical double-layer capacitance, and the value of C_{dl} is obtained from the slope of the current density *vs.* scan rate obtained from CV plots collected in the non-faradic region (1.14–1.22 V *vs.* RHE) at various scan rates.[93] Fig. 8a and S5† show the CV plots of Ni + Fe doped CeO_2 and other electrode catalysts collected at different scan rates. The current density *vs.* scan rates produces a straight line, and linear fit gives the slope value equal to C_{dl} (Fig. 8b). The calculated values of EASA for all catalysts are presented in Table 3. The EASA value of Ni + Fe doped sample was 60.8 cm^2, which was highest among all the electrodes. The observation revealed that more active sites for mesopores feature were available for the electrochemical reaction, leading to superior HER and OER performance.

The charge transfers phenomenon occurring at the electrode/electrolyte interface is a key parameter to analyze the electrocatalytic performance of as-synthesized materials. The potentiostatic EIS analysis were performed in the frequency range 100 kHz to 0.1 Hz at the initial DC voltage −0.2 V *vs.* RHE and 1.56 V *vs.* RHE for HER and OER studies, respectively. The Nyquist plot depicted in the Fig. 8(c and d) consist of a small semicircle at high frequency regime (catalyst/nickel foam and between catalyst, R_{ct1}) and larger semicircle at low frequency regime (interface of electrode and electrolyte, R_{ct2}) at the applied DC voltage.[17] The value of R_{ct2} at HER and OER kinetic for all the electrodes are generated by fitting the Nyquist plots with the equivalent circuit shown as inset in the Fig. 8c and d. The co-doped CeO_2 have smallest R_{ct2} 2.9 Ω cm^{-2} and 3.5 Ω cm^{-2} (Table 3) at HER and OER condition, suggesting faster charge-transfer and consequently a superior electrocatalytic performance for HER, and OER. The higher HER and OER

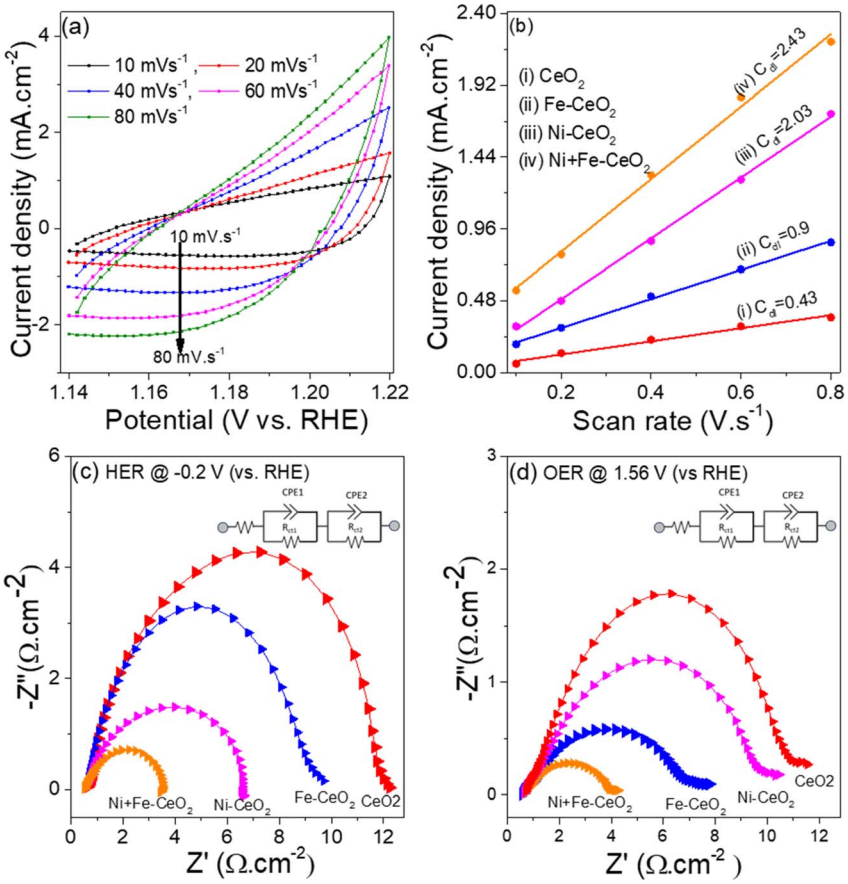

Fig. 8 (a) CV curves of Ni + Fe doped CeO_2 collected at different scan rates in non-faradic region (b) current density *vs.* scan rates (c) and (d) Nyquist plots of the synthesized materials at HER and OER. The inset in (c) and (d) represent the equivalent circuit diagram to fit the EIS data.

Table 3 The electrochemical activities of as-synthesized catalysts

Evaluated electrochemical properties such as η_{10}, EASA, R_{ct}					
Catalysts	HER $(\eta_{10})^a$ (mV)	OER $(\eta_{10})^a$ (mV)	EASA (cm^2)	R_{ct} (Ω cm^{-2}) for HER	R_{ct} (Ω cm^{-2}) for OER
CeO_2	198	470	10.6	11.5	10.7
Ni-CeO_2	123	450	50.7	6.0	9.6
Fe-CeO_2	157	420	22.5	9.1	6.9
Ni + Fe-CeO_2	**104**	**380**	**60.8**	**2.9**	**3.5**

[a] Reported in mV *vs.* RHE.

activities of Ni + Fe CeO_2 electrode compared to other prepared catalyst as well as literature suggest that co doped Ni, Fe could be a promising material to fulfil the future energy demand.

4. Conclusions

In summary, a sol–gel route was used to prepare pristine CeO_2 and 20 mol% metal cation(s) Ni + Fe, Ni, and Fe doped CeO_2 electrocatalysts. The presence of Ni + Fe co-dopant(s) altered the growth of CeO_2 resulting in a mesoporous structure with greater number of electrochemically active sites. Co-doped samples were also associated with greater concentration of O_V, a favourable condition for electrochemical water splitting reaction. The Ni + Fe co-doped CeO_2 electrode demonstrated superior HER and OER bifunctional activities in 1 M KOH electrolytes and required only 104 mV and 380 mV overpotentials for HER and OER to afford a current density of 10 mA cm^{-2}. The higher HER, and OER activities were the result of high electrochemical surface area (60.8) cm^2 and low charge transfer resistance. This work illustrates the impact of Ni, Fe co-doping on the microstructure and point defect (oxygen vacancy) as a tool for materials design of electrocatalyst based hydrogen production.

Data availability

Data included as part of the article ESI.† Additional data available upon reasonable request.

Conflicts of interest

There are no conflicts to declare.

Acknowledgements

The authors acknowledge support of the Center for Hierarchical Waste Form Materials, an Energy Frontier Research Center funded by the U.S. Department of Energy, Office of Science, Basic Energy Sciences (DE-SC0016574). A portion of this research using Raman spectroscopy was performed using funding received from the DOE Office of Nuclear Energy's Nuclear Energy University Program under Award Number DE-NE0009314.

References

1 M. S. Dresselhaus and I. L. Thomas, *Nature*, 2001, **414**, 332–337.
2 Z. W. Seh, J. Kibsgaard, C. F. Dickens, I. Chorkendorff, J. K. Nørskov and T. F. Jaramillo, *Science*, 2017, **355**, 1–12.
3 J. Jiang, F. Sun, S. Zhou, W. Hu, H. Zhang, J. Dong, Z. Jiang, J. Zhao, J. Li, W. Yan and M. Wang, *Nat. Commun.*, 2018, **9**, 2885.
4 H. Sun, X. Xu, H. Kim, W. Jung, W. Zhou and Z. Shao, *Energy Environ. Mater.*, 2023, **6**, e12441.
5 Y. Liu, X. Wang, M. Yang, Y. Li, Y. Xiao and J. Zhao, *Nanoscale*, 2023, **15**, 17936–17945.
6 H. Sun, X. Xu, Y. Song, W. Zhou and Z. Shao, *Adv. Funct. Mater.*, 2021, **31**, 2009779.
7 J. Wang, Y. Gao, H. Kong, J. Kim, S. Choi, F. Ciucci, Y. Hao, S. Yang, Z. Shao and J. Lim, *Chem. Soc. Rev.*, 2020, **49**, 9154–9196.
8 C. Wei, R. R. Rao, J. Peng, B. Huang, I. E. L. Stephens, M. Risch, Z. J. Xu and Y. Shao-Horn, *Adv. Mater.*, 2019, **31**, 1806296.
9 R. Bose, V. R. Jothi, K. Karuppasamy, A. Alfantazi and S. C. Yi, *J. Mater. Chem. A*, 2020, **8**, 13795–13805.
10 B. You and Y. Sun, *Acc. Chem. Res.*, 2018, **51**, 1571–1580.
11 Y. Li, Y. Sun, Y. Qin, W. Zhang, L. Wang, M. Luo, H. Yang and S. Guo, *Adv. Energy Mater.*, 2020, **10**, 1903120.
12 H.-J. Liu, R.-N. Luan, L.-Y. Li, R.-Q. Lv, Y.-M. Chai and B. Dong, *Chem. Eng. J.*, 2023, **461**, 141714.
13 Q. Shi, C. Zhu, D. Du and Y. Lin, *Chem. Soc. Rev.*, 2019, **48**, 3181–3192.
14 P. Zhai, Y. Zhang, Y. Wu, J. Gao, B. Zhang, S. Cao, Y. Zhang, Z. Li, L. Sun and J. Hou, *Nat. Commun.*, 2020, **11**, 5462.
15 L. Ji, J. Wang, X. Teng, T. J. Meyer and Z. Chen, *ACS Catal.*, 2020, **10**, 412–419.
16 X. Hu, Y. Gao, X. Luo, J. Xiong, P. Chen and B. Wang, *Nanoscale*, 2024, **16**, 4909–4918.
17 L. Li, B. Wang, G. Zhang, G. Yang, T. Yang, S. Yang and S. Yang, *Adv. Energy Mater.*, 2020, **10**, 2001600.
18 D. R. Ou, T. Mori, H. Togasaki, M. Takahashi, F. Ye and J. Drennan, *Langmuir*, 2011, **27**, 3859–3866.
19 N. Maheswari and G. Muralidharan, *Dalton Trans.*, 2016, **45**, 14352–14362.
20 H. T. Das, E. B. T, S. Dutta, N. Das, P. Das, A. Mondal and M. Imran, *J. Energy Storage*, 2022, **50**, 104643.

21 B. Wang, B. Zhu, S. Yun, W. Zhang, C. Xia, M. Afzal, Y. Cai, Y. Liu, Y. Wang and H. Wang, *NPG Asia Mater.*, 2019, **11**, 51.
22 J. Y. Cheon, J. H. Kim, J. H. Kim, K. C. Goddeti, J. Y. Park and S. H. Joo, *J. Am. Chem. Soc.*, 2014, **136**, 8875–8878.
23 Z. Chen, T. Ma, W. Wei, W.-Y. Wong, C. Zhao and B.-J. Ni, *Adv. Mater.*, 2024, 2401568.
24 Z.-H. Yang, S. Ren, Y. Zhuo, R. Yuan and Y.-Q. Chai, *Anal. Chem.*, 2017, **89**, 13349–13356.
25 K. Cui, C. Zhou, B. Zhang, L. Zhang, Y. Liu, S. Hao, X. Tang, Y. Huang and J. Yu, *ACS Appl. Mater. Interfaces*, 2021, **13**, 33937–33947.
26 Y.-H. Zhou, S. Wang, Y. Wan, J. Liang, Y. Chen, S. Luo and C. Yong, *J. Alloys Compd.*, 2017, **728**, 902–909.
27 M. Zhu, Y. Wen, L. Shi, Z. Tan, Y. Shen, K. Yin and L. Sun, *Nanoscale*, 2022, **14**, 11963–11971.
28 H. Qi, C. Shi, X. Jiang, M. Teng, Z. Sun, Z. Huang, D. Pan, S. Liu and Z. Guo, *Nanoscale*, 2020, **12**, 19112–19120.
29 Y. Wang, C. Meng, L. Zhao, J. Zhang, X. Chen and Y. Zhou, *Chem. Commun.*, 2023, **59**, 8644–8659.
30 D. A. Rakov, *Energy Adv.*, 2023, **2**, 235–251.
31 R. Wu, J. Xu, C.-L. Zhao, X.-Z. Su, X.-L. Zhang, Y.-R. Zheng, F.-Y. Yang, X.-S. Zheng, J.-F. Zhu, J. Luo, W.-X. Li, M.-R. Gao and S.-H. Yu, *Nat. Commun.*, 2023, **14**, 2306.
32 C.-F. Li, J.-W. Zhao, L.-J. Xie, J.-Q. Wu and G.-R. Li, *Appl. Catal., B*, 2021, **291**, 119987.
33 W. Liu, P. Geng, S. Li, W. Liu, D. Fan, H. Lu, Z. Lu and Y. Liu, *J. Energy Chem.*, 2021, **55**, 17–24.
34 R.-Y. Fan, J.-Y. Xie, H.-J. Liu, H.-Y. Wang, M.-X. Li, N. Yu, R.-N. Luan, Y.-M. Chai and B. Dong, *Chem. Eng. J.*, 2022, **431**, 134040.
35 G. Hai, J. Huang, L. Cao, K. Kajiyoshi, L. Wang, L. Feng, Y. Liu and L. Pan, *Dalton Trans.*, 2021, **50**, 11604–11609.
36 N. Qadeer, N. Jabeen, L. U. Khan, M. Sohail, M. Zaheer, M. Vaqas, A. Kanwal, F. Sajid, S. Qamar and Z. Akhter, *RSC Adv.*, 2022, **12**, 15564–15574.
37 S. Colis, A. Bouaine, G. Schmerber, C. Ulhaq-Bouillet, A. Dinia, S. Choua and P. Turek, *Phys. Chem. Chem. Phys.*, 2012, **14**, 7256–7263.
38 V. D. Araújo, W. Avansi, H. B. de Carvalho, M. L. Moreira, E. Longo, C. Ribeiro and M. I. B. Bernardi, *CrystEngComm*, 2012, **14**, 1150–1154.
39 P. Tamizhdurai, S. Sakthinathan, S.-M. Chen, K. Shanthi, S. Sivasanker and P. Sangeetha, *Sci. Rep.*, 2017, **7**, 46372.
40 K. Polychronopoulou, A. A. AlKhoori, A. M. Efstathiou, M. A. Jaoude, C. M. Damaskinos, M. A. Baker, A. Almutawa, D. H. Anjum, M. A. Vasiliades, A. Belabbes, L. F. Vega, A. F. Zedan and S. J. Hinder, *ACS Appl. Mater. Interfaces*, 2021, **13**, 22391–22415.
41 P. Venkataswamy, D. Jampaiah, A. E. Kandjani, Y. M. Sabri, B. M. Reddy and M. Vithal, *Res. Chem. Intermed.*, 2018, **44**, 2523–2543.
42 W. Zhan, S. Yang, P. Zhang, Y. Guo, G. Lu, M. F. Chisholm and S. Dai, *Chem. Mater.*, 2017, **29**, 7323–7329.
43 C. C. L. McCrory, S. Jung, J. C. Peters and T. F. Jaramillo, *J. Am. Chem. Soc.*, 2013, **135**, 16977.
44 T. Mathew, K. Sivaranjani, E. S. Gnanakumar, Y. Yamada, T. Kobayashi and C. S. Gopinath, *J. Mater. Chem.*, 2012, **22**, 13484–13493.
45 S. Niu, S. Li, Y. Du, X. Han and P. Xu, *ACS Energy Lett.*, 2020, **5**, 1083–1087.
46 Y. Wang, G. Qian, Q. Xu, H. Zhang, F. Shen, L. Luo and S. Yin, *Appl. Catal., B*, 2021, **286**, 119881.
47 M. Xiao, D. Han, X. Yang, N. Tsona Tchinda, L. Du, Y. Guo, Y. Wei, X. Yu and M. Ge, *Appl. Catal., B*, 2023, **323**, 122173.
48 X. Mei, X. Zhao, Y. Chen, B. Deng, Q. Geng, Y. Cao, Y. Li and F. Dong, *ACS Sustain. Chem. Eng.*, 2023, **11**, 15609–15619.
49 X. Xu, L. Liu, Y. Tong, X. Fang, J. Xu, D. Jiang and X. Wang, *ACS Catal.*, 2021, **11**, 5762–5775.
50 B. Liu, B. Liu, Q. Li, Z. Li, M. Yao, R. Liu, X. Zou, H. Lv, W. Wu, W. Cui, Z. Liu, D. Li, B. Zou, T. Cui and G. Zou, *Phys. Status Solidi*, 2011, **248**, 1154–1157.
51 R. Murugan, G. Ravi, G. Vijayaprasath, S. Rajendran, M. Thaiyan, M. Nallappan, M. Gopalan and Y. Hayakawa, *Phys. Chem. Chem. Phys.*, 2017, **19**, 4396–4404.
52 Z. Zou, T. Zhang, L. Lv, W. Tang, G. Zhang, R. K. Gupta, Y. Wang and S. Tang, *ACS Sustain. Chem. Eng.*, 2023, **11**, 7443–7453.
53 K. Brinkman, E. B. Fox, P. Korinko, R. Lascola, Q. Liu and F. Chen, *MRS Online Proc. Libr.*, 2010, **1256**, 1230–1256.
54 B. Liu, C. Li, G. Zhang, L. Yan and Z. Li, *New J. Chem.*, 2017, **41**, 12231–12240.
55 L. Minervini, M. O. Zacate and R. W. Grimes, *Solid State Ionics*, 1999, **116**, 339–349.
56 W. D. Kingery, H. K. Bowen and D. R. Uhlmann, *Introduction to Ceramics*, John wiley & sons, 1976, vol. 17.
57 O. H. Laguna, M. A. Centeno, M. Boutonnet and J. A. Odriozola, *Appl. Catal., B*, 2011, **106**, 621–629.
58 G. Li, R. L. Smith and H. Inomata, *J. Am. Chem. Soc.*, 2001, **123**, 11091–11092.
59 C. Liang, Z. Ma, H. Lin, L. Ding, J. Qiu, W. Frandsen and D. Su, *J. Mater. Chem.*, 2009, **19**, 1417–1424.
60 D. Jampaiah, T. Srinivasa Reddy, A. E. Kandjani, P. R. Selvakannan, Y. M. Sabri, V. E. Coyle, R. Shukla and S. K. Bhargava, *J. Mater. Chem. B*, 2016, **4**, 3874–3885.
61 H. Wang and G. Tsilomelekis, *Catal. Sci. Technol.*, 2020, **10**, 4362–4372.
62 X. Chen, S. Zhan, D. Chen, C. He, S. Tian and Y. Xiong, *Appl. Catal., B*, 2021, **286**, 119928.
63 L. Zhang, Y. Jiang, K. Zhu, N. Shi, Z. U. Rehman, R. Peng and C. Xia, *Small Methods*, 2024, 2301686.
64 H. Bao, X. Chen, J. Fang, Z. Jiang and W. Huang, *Catal. Lett.*, 2008, **125**, 160–167.
65 P. S. Murphin Kumar, S. Thiripuranthagan, T. Imai, G. Kumar, A. Pugazhendhi, S. R. Vijayan, R. Esparza, H. Abe and S. K. Krishnan, *ACS Sustain. Chem. Eng.*, 2017, **5**, 11290–11299.
66 C. Yang, F. Bebensee, J. Chen, X. Yu, A. Nefedov and C. Wöll, *ChemPhysChem*, 2017, **18**, 1874–1880.
67 Q. Sun, Y. Liu, X. Li, X. Guo, W.-H. Huang, Y. Zhu, Z. Wang, C.-C. Chueh, C.-L. Chen, Y.-K. Peng and Z. Zhu, *Energy Fuels*, 2023, **37**, 9434–9443.

68 S. Kato, M. Ammann, T. Huthwelker, C. Paun, M. Lampimäki, M.-T. Lee, M. Rothensteiner and J. A. van Bokhoven, *Phys. Chem. Chem. Phys.*, 2015, **17**, 5078–5083.
69 C. Yang, F. Bebensee, J. Chen, X. Yu, A. Nefedov and C. Wöll, *ChemPhysChem*, 2017, **18**, 1957.
70 M. Cheng, H. Fan, Y. Song, Y. Cui and R. Wang, *Dalton Trans.*, 2017, **46**, 9201–9209.
71 A. Punnoose, K. Dodge, J. J. Beltrán, K. M. Reddy, N. Franco, J. Chess, J. Eixenberger and C. A. Barrero, *J. Appl. Phys.*, 2014, **115**, 17B534.
72 Y. Xue, L. Hui, H. Yu, Y. Liu, Y. Fang, B. Huang, Y. Zhao, Z. Li and Y. Li, *Nat. Commun.*, 2019, **10**, 2281.
73 M.-C. Sung, G.-H. Lee and D.-W. Kim, *J. Alloys Compd.*, 2019, **800**, 450–455.
74 L. Zhou, P. He, T. Yang, S. Chen, Q. He, F. Dong, L. Jia, H. Zhang, B. Jia and X. He, *Int. J. Hydrogen Energy*, 2020, **45**, 28682–28695.
75 J. Rashid, N. Parveen, T. ul Haq, A. Iqbal, S. H. Talib, S. U. Awan, N. Hussain and M. Zaheer, *ChemCatChem*, 2018, **10**, 5587–5592.
76 S. Swathi, R. Yuvakkumar, P. Senthil Kumar, G. Ravi, M. Thambidurai, C. Dang and D. Velauthapillai, *Fuel*, 2022, **310**, 122319.
77 Q. Zhou, S. Liu, Y. Zhang, Z. Zhu, W. Su and M. Sheng, *Ceram. Int.*, 2020, **46**, 20871–20877.
78 L. Gui, Z. Wang, K. Zhang, B. He, Y. Liu, W. Zhou, J. Xu, Q. Wang and L. Zhao, *Appl. Catal., B*, 2020, **266**, 118656.
79 L. Tian, H. Liu, B. Zhang, Y. Liu, S. Lv, L. Pang and J. Li, *ACS Appl. Nano Mater.*, 2022, **5**, 1252–1262.
80 L. Tian, H. Liu, X. Yi, X. Wang, L. Pang and J. Li, *Int. J. Hydrogen Energy*, 2023, **48**, 23831–23841.
81 Y. Yu, Y. Liu, X. Peng, X. Liu, Y. Xing and S. Xing, *Sustainable Energy Fuels*, 2020, **4**, 5156–5164.
82 Y.-N. Zhou, Y.-W. Dong, Y. Wu, B. Dong, H.-J. Liu, X.-J. Zhai, G.-Q. Han, D.-P. Liu and Y.-M. Chai, *Chem. Eng. J.*, 2023, **463**, 142380.
83 C. Hu, L. Zhang and J. Gong, *Energy Environ. Sci.*, 2019, **12**, 2620–2645.
84 H. Lin, W. Zhang, Z. Shi, M. Che, X. Yu, Y. Tang and Q. Gao, *ChemSusChem*, 2017, **10**, 2597–2604.
85 M. Ji, W. Yaseen, H. Mao, C. Xia, Y. Xu, S. Meng, J. Xie and M. Xie, *Inorg. Chem.*, 2023, **62**, 12383–12391.
86 E. Demir, S. Akbayrak, A. M. Önal and S. Özkar, *J. Colloid Interface Sci.*, 2019, **534**, 704–710.
87 Y. Yu, X. Peng, U. Ali, X. Liu, Y. Xing and S. Xing, *Inorg. Chem. Front.*, 2019, **6**, 3255–3263.
88 D. Ghosh and D. Pradhan, *Langmuir*, 2023, **39**, 3358–3370.
89 Y. Tuo, X. Wang, C. Chen, X. Feng, Z. Liu, Y. Zhou and J. Zhang, *Electrochim. Acta*, 2020, **335**, 135682.
90 S. Paladugu, I. M. Abdullahi, H. Singh, S. Spinuzzi, M. Nath and K. Page, *ACS Appl. Mater. Interfaces*, 2024, **16**, 7014–7025.
91 J. Yu, J. Wang, X. Long, L. Chen, Q. Cao, J. Wang, C. Qiu, J. Lim and S. Yang, *Adv. Energy Mater.*, 2021, **11**, 2002731.
92 N. K. Shrestha, S. A. Patil, J. Han, S. Cho, A. I. Inamdar, H. Kim and H. Im, *J. Mater. Chem. A*, 2022, **10**, 8989–9000.
93 Y.-N. Zhou, W.-L. Yu, Y.-N. Cao, J. Zhao, B. Dong, Y. Ma, F.-L. Wang, R.-Y. Fan, Y.-L. Zhou and Y.-M. Chai, *Appl. Catal., B*, 2021, **292**, 120150.